

Atomic Scale Surface Structure and Morphology of InAs Nanowire Crystal Superlattices: The Effect of Epitaxial Overgrowth

J. V. Knutsson,[†] S. Lehmann,[†] M. Hjort,[†] P. Reinke,[‡] E. Lundgren,[†] K. A. Dick,^{†,§} R. Timm,[†] and A. Mikkelsen^{*,†}

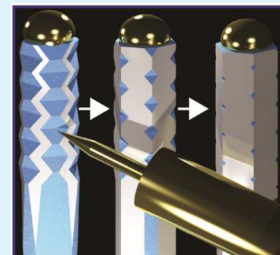
[†]Department of Physics and The Nanometer Structure Consortium, Lund University, P.O. Box 118, 22 100 Lund, Sweden

[‡]Department of Materials Science and Engineering, University of Virginia, 395 McCormick Road, Charlottesville, Virginia 22904, United States

[§]Center for Analysis and Synthesis, Lund University, P.O. Box 124, 221 00 Lund, Sweden

Supporting Information

ABSTRACT: While shell growth engineering to the atomic scale is important for tailoring semiconductor nanowires with superior properties, a precise knowledge of the surface structure and morphology at different stages of this type of overgrowth has been lacking. We present a systematic scanning tunneling microscopy (STM) study of homoepitaxial shell growth of twinned superlattices in zinc blende InAs nanowires that transforms $\{111\}$ A/B-type facets to the nonpolar $\{110\}$ -type. STM imaging along the nanowires provides information on different stages of the shell growth revealing distinct differences in growth dynamics of the crystal facets and surface structures not found in the bulk. While growth of a new surface layer is initiated simultaneously (at the twin plane interface) on the $\{111\}$ A and $\{111\}$ B nanofacets, the step flow growth proceeds much faster on $\{111\}$ A compared to $\{111\}$ B leading to significant differences in roughness. Further, we observe that the atomic scale structures on the $\{111\}$ B facet is different from its bulk counterpart and that shell growth on this facet occurs via steps perpendicular to the $\langle 112 \rangle$ B-type directions.



KEYWORDS: STM, nanowire, surface, III–V, InAs, homoepitaxy, shell growth

INTRODUCTION

III–V semiconductor nanowires (NWs) with highly controlled structural and compositional heterostructures not only play an important role for fundamental research^{1,2} but also have proven performance potential for devices within electronics,^{3,4} photonics,^{5,6} and energy harvesting.^{6,7} A critical factor in the development of NW devices is epitaxial shell growth (overgrowth) as it adds another engineering dimension by providing the option to create radial variations in composition or doping.^{8,9} Shell growth control is complicated by a number of effects such as undesired tapering and unwanted radial doping.¹⁰ Still, for example, anisotropic overgrowth due to polarity differences between NW sidewall facets^{11,12} can be used to engineer novel NW sidewall decorations such as self-assembled quantum dots (QDs).⁹

In analogy to the well-studied 2D planar epitaxial heterostructure formation, NW shell growth beyond trial-and-error engineering requires an intimate understanding of nucleation sites, growth speeds, and interplay between neighboring facets to achieve the desired shell structure. Also of importance are dynamic features such as any variations of the ratio between layer nucleation and step flow growth. To further complicate matters, atomic scale precision is needed to avoid unwanted defect formation, and the growth should therefore be studied with subnanometer resolution. Such high precision studies have until now exclusively been carried out using high resolution transmission electron microscopy (HRTEM). This

technique has provided great insights into shell growth but only allows the side or topview profiles of the NWs to be studied. However, detailed studies of NW surfaces can be conducted with scanning tunneling microscopy (STM) which is capable of resolving individual surface atoms. We present the first systematic study of the morphology and overgrowth of the V-groove shapes of twin plane superlattices (TSLs), made possible by our growth capabilities in combination with our surface science analytical tools.^{13–17}

Systematic surface studies of NW sidewall growth are especially relevant as the limited size of their facets can result in behavior not found for “infinite” planar surfaces. In addition, NWs often show crystal structures different from the thermodynamically stable zinc blende (Zb), such as the wurtzite (Wz) structure or random stacking. Investigating such structures is interesting not only because it can enhance our fundamental understanding of NW shell growth but also because it is highly relevant for NW electronics devices since NW device performance has been shown to be strongly influenced by surface morphology and surface defects.^{10,16,18–20} Since NWs can exhibit complex surface geometries such as the sawtooth shaped sidewalls emerging in TSLs,^{21,22} consisting of alternating $\{111\}$ A- and $\{111\}$ B-type nanofacets, it is possible

Received: November 12, 2014

Accepted: February 24, 2015

Published: February 24, 2015

to study atomically precise V-shaped grooves. The effects on growth processes due to the corner geometry of such grooves have been discussed,^{10,23–28} but no surface studies with atomic precision have been conducted. In addition, detailed understanding of the overgrowth mechanics of TSLs would allow for positioning control of QDs.²⁹

In this work, we present STM studies of the homoepitaxial overgrowth of the V-grooves between {111}A and {111}B facets of Zb TSL InAs NWs. Growing InAs NWs often results in natural tapering, i.e., radial growth by material incorporation on the NW sidewalls in parallel to the intended axial growth. As a result, a gradient in overgrowth (shell) is formed along the NW growth axis with little shell growth having occurred nearest to the axial growth front (at the seed particle) but substantial overgrowth at the bottom of the NW. By imaging along the NW, information on different stages in the overgrowth process could be obtained, allowing us to gain insight into the transition from the initial sawtooth {111}A/B-type facet morphology of Zb TSL to smooth {110}-type facets;¹⁵ see Figure 1B,C. The high resolution of STM allows for imaging of single atomic steps as well as of individual atoms on the NW facets, providing a detailed picture of the overgrowth process.

EXPERIMENTAL SECTION

The NWs were grown on an InAs(111)B substrate in a metal–organic vapor phase epitaxy (MOVPE) reactor using Au particles to seed the growth. 80 nm Au particles with an areal density of 0.5 and $1.0 \mu\text{m}^{-2}$ were deposited using an aerosol technique.³⁰ A 10 min anneal at 550°C , in an AsH_3/H_2 atmosphere, was performed prior to growth in

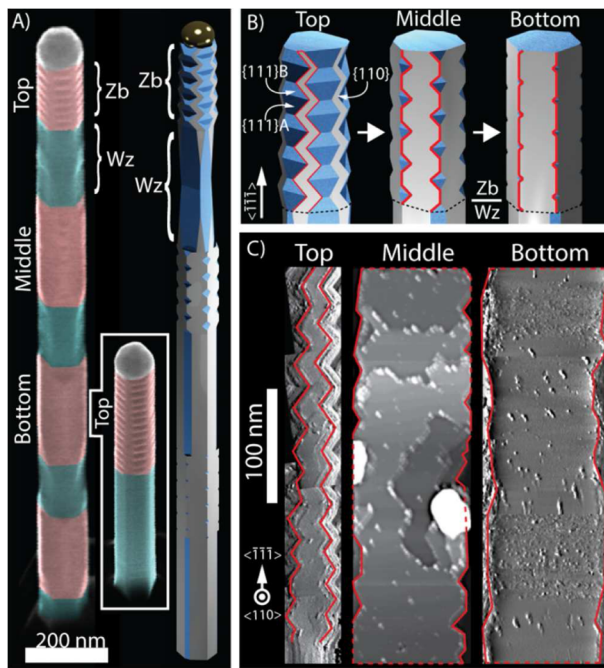


Figure 1. (A) 30° degree tilted view scanning electron micrograph, color coded for Zb (red) and Wz (green) parts, as well as a model NW. Inset shows a NW with 1 Zb segment in scale with the main image. (B) Illustration of Zb TSL in different stages of overgrowth, displaying the {111}A/B-type facets (blue) as well as the {110}-type overgrowth facets (gray with red borders). (C) STM images of {110} facet from the top, middle, and bottom Zb segment, respectively. Top and bottom image have been differentiated to make height variations more clearly visible. $U = -1.6 \text{ V}$, $I = 100 \text{ pA}$ for top image and $U = -1.0 \text{ V}$, $I = 50 \text{ pA}$ for middle and bottom.

order to remove surface oxides. Following this, the temperature was set to the growth temperature of 460°C , and upon thermal stabilization, growth was initiated. Growth material was supplied via trimethylindium (TMIn) and arsine (AsH_3) precursors. The growth was executed in an AIXTRON 200/4 system using a total reactor flow of 13 standard liters per minute (slm) at a total reactor pressure of 100 mbar. Postprocessing involved cooling in an AsH_3/H_2 atmosphere in order to avert thermal decomposition of the NWs. The crystal structure was tuned along the NW by altering the V/III-precursor flow ratio as described in refs 31 and 32.

The NWs were transferred to an n-doped epi-ready InAs (111)B substrate by mechanical break-off¹⁴ and loaded into vacuum. Removal of native oxides, formed after transport in air, was performed by annealing the samples at 380°C in an atomic hydrogen atmosphere with a pressure of 2×10^{-6} mbar for 20–40 min. This has been proven to be a suitable way to clean III–V NWs.^{13,14} Importantly, this deoxidation procedure was found to remove the native oxides while preserving the general step structure and resulting in no new atomic scale reconstructions on the surface; see the Supporting Information for more details.

The oxide free NWs were investigated using an Omicron XA STM operated in ultrahigh vacuum (UHV, $p < 10^{-9}$ mbar) at room temperature. The STM was operated in constant current mode, and the set point current and sample bias will be denoted by I and U , respectively. Electrochemically etched W-tips that were cleaned and sharpened by in situ Ar-sputtering were used throughout the study.

This study is based on data from two different types of NW samples, having either 1 or 4 Zb segments. After NW break-off, the two samples usually oriented themselves differently on the substrate such that NWs with 1 Zb segment had {111}A/B-type facets facing upward whereas the 4 Zb segment sample oriented itself with the {110}-type facets facing up. In Figure 1A, scanning electron micrographs of typical NWs from both samples and a model NW can be seen. The crystal structure of each segment was confirmed using TEM as well as atomically resolved STM images.

RESULTS AND DISCUSSION

STM observations of the top Zb segment (see Figure 2A) reveal alternating {111}A- and {111}B-type facets along the

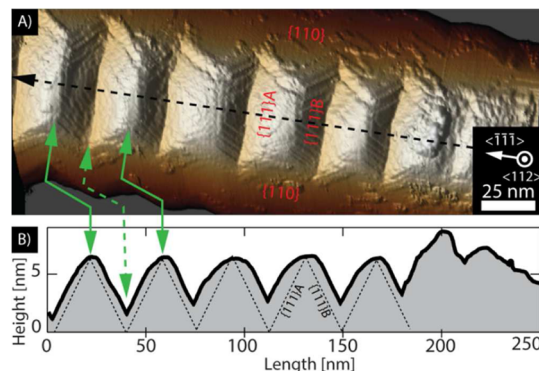


Figure 2. (A) STM image represented in 3D of a top Zb segment seen from a $\langle 112 \rangle$ -type direction. The convex and concave {111}A/B interfaces are marked with solid and dashed (both green) arrows, respectively. $U = -1.0 \text{ V}$, $I = 50 \text{ pA}$. (B) Line profile along the $[-1-1-1]$ direction of the Zb segment, as marked by the black dashed arrow in (A).

$[-1-1-1]$ growth axis in {112}-equivalent planes of the NW sidewalls, resulting in a sawtooth like shape of the Zb segment. The angle between {111}A/B-type facets and the $[-1-1-1]$ growth axis was measured to be 20° in the STM topography images, which is in agreement with the expected 19.5° . Every interface between adjacent {111}A/B-type facets corresponds

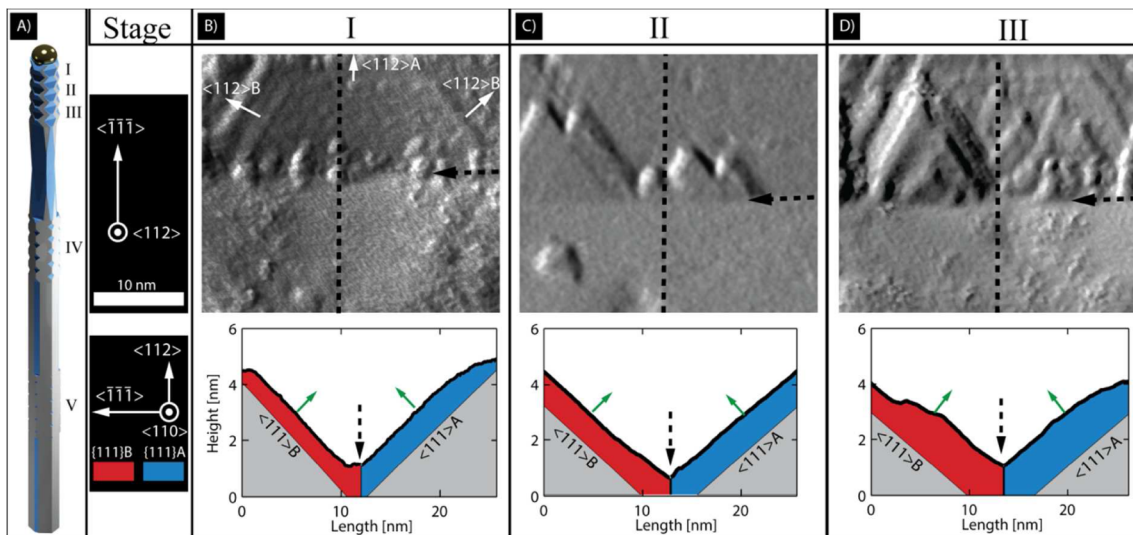


Figure 3. (A) Model of NW illustrating where different overgrowth stages in general were found along the NW. (B–D) STM images and line profiles of the top Zb segment in overgrowth stages I–III. The images have been differentiated to make the height variations more clearly visible. (B) Concave interface between adjacent $\{111\}$ A-type (bottom) and $\{111\}$ B-type facets (top) representative for stage I with the twin plane marked as a black dashed arrow. The round 2 nm sized features along the interface line correspond to unintentional material deposition from the STM tip. The position of the line profile is marked by the black dashed line. The red and blue areas in the line profiles represent relative overgrowth on $\{111\}$ B and $\{111\}$ A, respectively, with the gray area corresponding to ideal $\{111\}$ A/B-type facets without overgrowth, $U = -1.6$ V, $I = 150$ pA. (C) $\{111\}$ A/B-type facets in stage II. The small island on the $\{111\}$ A-type facet was deposited by the STM tip, $U = -1.7$ V, $I = 100$ pA. (D) $\{111\}$ A/B-type facets in stage III, $U = -1.6$ V, $I = 150$ pA.

to a twin plane. As shown in Figure 2A,B, two types of interfaces can be identified, concave interfaces (twin plane in the bottom of a groove) and convex interfaces (twin planes on the ridges of the sawtooth structure). Adjacent to the sawtooth structure in Figure 2A, with a relative rotation of 30° around the $[-1-1-1]$ axis, thin zigzag shaped $\{110\}$ -type facets can be seen. Their presence has been attributed to overgrowth,¹⁵ and the zigzag shape of the facet edge comes as a result of a 60° rotation of the crystal symmetry with respect to the growth axis, occurring at each twin plane position.

For NWs grown in the $[-1-1-1]$ direction, the In-terminated $\{111\}$ A-type facets of the NW sidewalls will be facing upward and the As-terminated $\{111\}$ B-type facets face downward with respect to the growth direction. The growth direction was determined by locating the Au seed particle, making it possible to identify the $\{111\}$ A/B-type facets directly.

When traversing along the NW (thus imaging the V-grooves at different stages of overgrowth), five distinct surface morphologies could be identified for the $\{111\}$ A/B-type facets, denoted as stages I–V. Each stage represents later and later times in the overgrowth process (stage I being the earliest, i.e., the part closest to the Au-particle); see Figure 3A. Stages IV and V were generally observed in the middle and bottom segments of the 4 Zb segment NW sample; see Figure 1A.

The type I morphology, depicted in Figure 3B, could only be identified within the first few twin planes closest to the Au particle corresponding to very limited overgrowth. In this stage, the $\{111\}$ A-type facets are atomically flat without island formation or noncomplete overgrowth layers (individual atomic layers from the shell growth). However, step bunching is found toward the convex interface as indicated by a rounded shape of the line profiles at such positions. The relative amount of overgrowth between the $\{111\}$ A/B-type facets can be estimated from a line profile by identifying the positions of the concave and convex interfaces. An original, nonovergrown, $\{111\}$ A/B-type facet can then be approximated by interpolating a line

(along $\langle 111 \rangle$ -type directions) between the concave and convex interfaces. The difference between the line profile and the estimated original facet is assumed to be a result of overgrowth. Using this method, it can be seen from Figure 3B that the overgrown film is thicker on the $\{111\}$ A-type facet compared to the $\{111\}$ B-type facet, indicative of a lower growth on the $\{111\}$ B-type facet. In line profiles, across the two facets (as is normally observed in HRTEM), they appear quite similar in roughness at this stage, but from the STM top view, we can see that the $\{111\}$ B-type facets have steps toward the interfaces of the adjacent $\{110\}$ -type facets in two $\langle 112 \rangle$ B-type directions; thus, in fact, the $\{111\}$ B-type is more rough already at this stage.

In stage II, represented in Figure 3C, the surface morphology of the $\{111\}$ A-type facets is equivalent to the stage I morphology. When comparing the $\{111\}$ B-type facet in stages I and II, several islands having the shape of one or more merged triangles can be seen in stage II, which was not observed in stage I. The triangle shaped layers, all having a common base at the concave interface, have steps in the $\langle 112 \rangle$ B-type directions and corners pointing in the $\langle 112 \rangle$ A-type directions. These layers are assumed to be newly formed (incomplete) overgrowth layers on the $\{111\}$ B-type facet. Since these newly formed layers all have a common base at the concave twin interface, it is suggested that nucleation of overgrowth layers on the $\{111\}$ B-type facets always is initiated at this position. It has been proposed previously that the corner geometry of the concave interface favors nucleation.^{10,23–25} Our study strongly suggests that this interface is the preferred site of nucleation for the overgrowth and that growth occurs exclusively as steps in the $\langle 112 \rangle$ B-type directions.

No islands could be observed on either the $\{111\}$ A- or $\{111\}$ B-type facets that did not have a base at the concave interface, and we suggest that overgrowth layers on both facets grow via step flow growth once nucleation has occurred at the concave interface. The triangular shape of overgrowth layers on

the $\{111\}$ B-type facet shows that the step flow growth occurs along steps perpendicular to the $\langle 112 \rangle$ B-, no steps perpendicular to the $\langle 112 \rangle$ A-type directions are observed. This can be explained by the different atomic scale termination of $\langle 112 \rangle$ A/B-oriented step edges. A similar behavior has been observed previously for metallic homoepitaxy on 2D surfaces³³ and is in agreement with observations on H-cleaned $\{111\}$ B wafers, where triangular islands also were observed.³⁴ No incomplete overgrowth layers were observed on $\{111\}$ A-type facets suggesting a very rapid growth relative the $\{111\}$ B-type facets in the $\langle 112 \rangle$ -equivalent directions. We note that this growth mode actually leads to a situation where the profiles of both facets, as observed in Figure 3B, will look smooth, while the top view reveals a considerable roughening perpendicular to the NW growth direction.

In stage III, see Figure 3D, additional triangular layers have formed on the $\{111\}$ B-type facets such that many monolayers are visible. The areas of these new triangular layers are small compared to the area of layers observed in stages I and II. Although the concave interface itself is still well-defined, the multitude of layers makes the $\{111\}$ B-type facet appear somewhat disordered. The curved shape of the $\{111\}$ A-type is even more pronounced, making it hard to clearly define the position of the twin plane at the convex interface. The $\{111\}$ A-type facet, however, exhibits no steps and can still be considered as atomically flat. Despite the many incomplete layers observed on the $\{111\}$ B-type facet, the number of overgrowth layers on the $\{111\}$ A- and $\{111\}$ B-type facets are found to be equal at the concave interface for stages I–IV, as seen in corresponding line profiles of Figures 3B–D and 4B. This suggests that growth of new layers on the $\{111\}$ A/B-type facets is coupled, i.e., initiated on both facets simultaneously and from the same nucleus. In addition, many triangles can be seen on the $\{111\}$ B-type facet along a single interfacial line suggesting that several nucleation events occur for each overgrowth layer. This is consistent with the nucleation rate being fast compared to incorporation of growth material at the sides of the triangular facets. An estimate of the ratio between the step flow growth of the overgrowth layers on the $\{111\}$ B and the nucleation rate along the interface can be calculated by assuming that the size of a triangle is correlated to the time of nucleation; see the Supporting Information. We report a mean step flow growth progression per nucleation event, γ_s , of 2.0 ± 1.9 nm/event in the $\langle 112 \rangle$ B-type directions for stage II of the overgrowth.

The observation that the overgrowth layers on the $\{111\}$ B-type facets in stage I are more complete compared to stages II and III suggests that the growth rate is varying over time. The almost complete layers formed in stage I followed by gradually smaller layers formed in stages II and III indicate a decreasing step flow growth rate as the overgrowth proceeds, with large values of γ_s in stage I and gradually smaller values for later stages. There are two likely explanations for a nonlinear growth rate. It could either be as a result of a nonconstant nucleation rate, i.e., the time between nucleation events at the twin plane of the concave interface decrease over time resulting in new layers forming more and more rapidly, or due to a material limited growth. A nonconstant nucleation rate can be ruled out as it would give rise to a nonlinear growth of the $\{110\}$ facet, but a linear growth of the $\{110\}$ facet width was measured. The width of the $\{110\}$ facets and the depths of the V-groove pockets as well as the width of concave interface were measured along a top Zb segment. They all show a linear trend, indicating

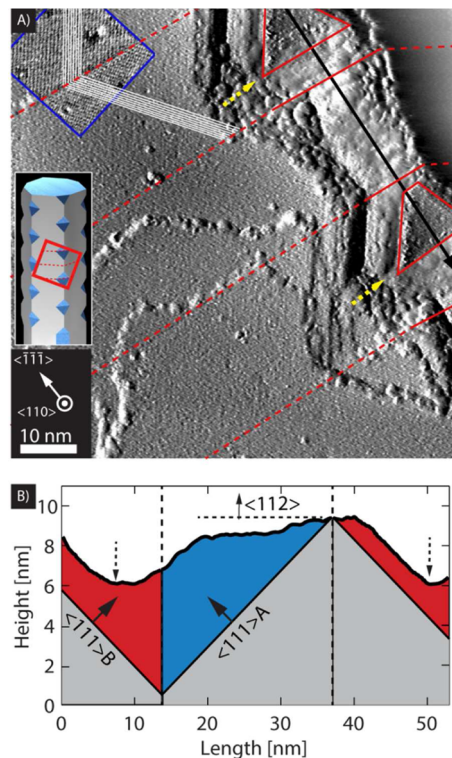


Figure 4. (A) STM image of Zb segment in stage IV viewed in a $\langle 110 \rangle$ -equivalent direction with both $\{110\}$, $\{111\}$ A-, and $\{111\}$ B-type facets visible. The image has been differentiated to make the height variations more clearly visible. Twin planes are marked by red dashed lines; dashed (yellow) arrows show the position of the bottom corner of the V-grooves. The blue square denotes a contrast enhanced inset image with visible atomic rows (white lines for guidance) on the $\{110\}$ -type surface. Black arrow defines the line profile show in (B). Red triangles show well-defined part of $\{111\}$ B facets. Inset (in black rectangle) illustrates the part of the NW that is shown in the main image. (B) Line profile from (A). Dashed arrows (black) show the bottom of the V-grooves. Vertical dashed lines (black) represent twin plane positions. The red and blue areas represent relative overgrowth on $\{111\}$ B and $\{111\}$ A, respectively, with the gray area corresponding to ideal $\{111\}$ A/B-type facets without overgrowth. $U = -1.9$ V, $I = 100$ pA.

that the rate of forming overgrowth layers on the facets must have been constant along the NW and thus over time (see the Supporting Information). Material limited growth explains the increase in number of incomplete overgrowth layers; a large number of layers will decrease the growth speed of each individual layer if the process is limited by material supply. Although there is a supersaturation in the catalyst particle, the material incorporation pathways for sidewall growth differs from Au-induced growth, and it is possible that the material reaching the $\{111\}$ B-type facets is limited due to a more favorable incorporation at the $\{111\}$ A-type facets. It can also be speculated that the vicinity of the catalyst particle gives rise to a gradient in material supply along the NW due to preferential collection of growth species in the Au-particle. Since complete layers on the $\{111\}$ A-type facets are observed for all stages of the growth, we assume that they are not affected by any significant supply limitations.

In stage IV, see Figure 4, generally found in the middle segment of the 4 Zb sample (see Figure 1A), the $\{110\}$ overgrowth facets dominate and only small $\{111\}$ -type facets remain as also illustrated in the model of Figure 1B. The

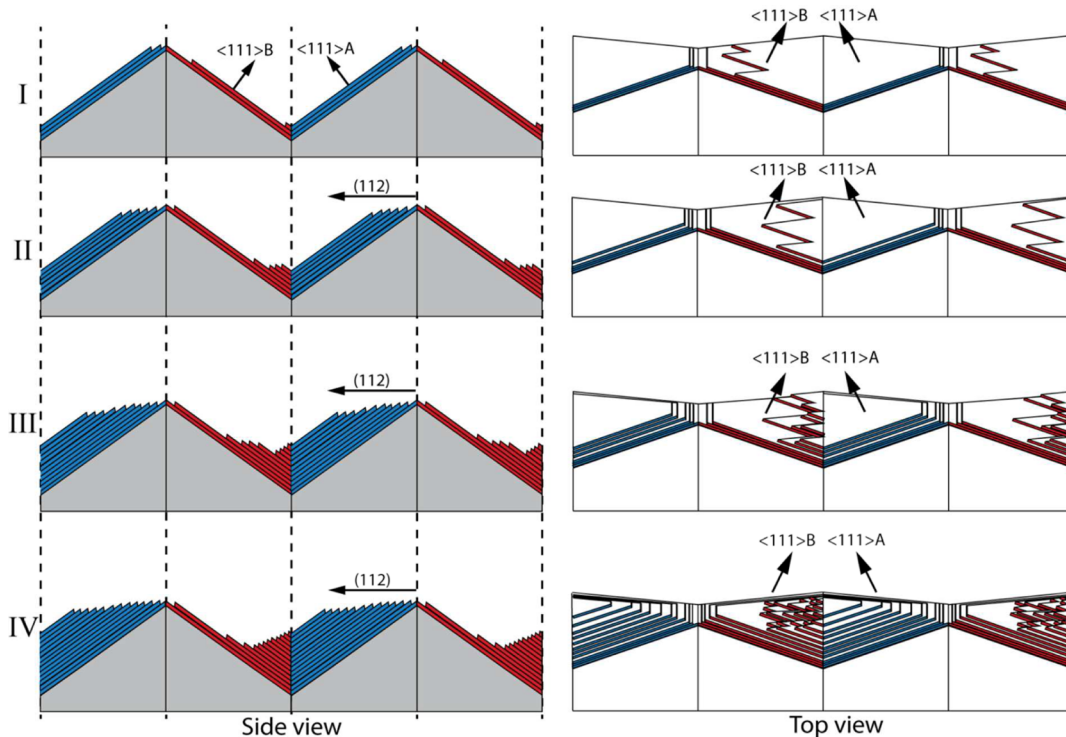


Figure 5. Illustration of the growth dynamics of the {111}-type facets, showing schematically stages I–IV from side view (left) and top view (right).

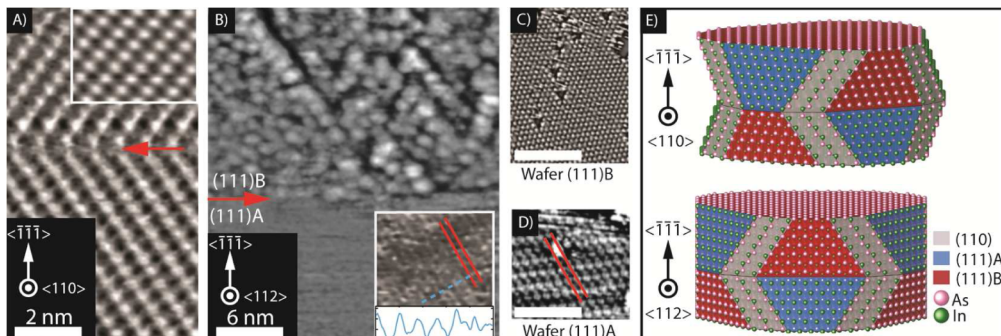


Figure 6. (A) Atomically resolved image of a twin boundary (red arrow) on a {110}-type facet of the NW, $U = -2.3$ V, $I = 100$ pA. Inset shows an analogously treated surface of an InAs(110) wafer, $U = -2.9$ V, $I = 200$ pA. (B) High resolution image of the {111}A/B-type facets (interface marked with red arrow) of a top Zb segment as observed in stages I–III. The image is differentiated for ease of viewing, $U = +1.1$ V, $I = 150$ pA. The inset shows a portion of the {111}A with enhanced contrast, same scale as main image, $U = -1.9$ V, $I = 150$ pA. (C) and (D) Depict corresponding {111}B- and {111}A-type surfaces from analogously treated InAs(111)A/B wafers, $U = -1.0$ V, $I = 50$ pA and $U = -2.0$ V, $I = 170$ pA, respectively. Same scale as in (B). (E) Depicts a basic atomic model, i.e., no surface reconstructions are shown, of a Zb twin plane in a NW illustrating the relative orientation of relevant surface planes.

{111}A-type facets appear as rough and disordered with poorly defined interfaces toward the adjacent {110}-type facets, whereas corresponding interfaces of the {111}B-type facets, at least partially, remain sharp and well-defined. Atomically resolved images reveal that the twin plane positions do not correlate with the bottom and ridge positions of the V-grooves in this stage of the overgrowth; see Figure 4. From the line profile of Figure 4B, it can be seen that the bottom corner of the V-groove has shifted along $[−1−1−1]$ and is now located on the {111}B-type facets and not as in previous stages at the twin planes of the concave interfaces. This shift is a continuous process throughout stages I–IV as illustrated in Figure 5 and is a consequence of the nonlinear growth rate on the {111}B facet, resulting in many incomplete overgrowth layers stacking on top of each other close to the concave interface. In analogy

to stages I–III, a similar amount of material can be found on both the {111}A- and {111}B-type facets at the twin plane of the concave interface, strongly suggesting that overgrowth layers on both facets nucleate at the twin planes. This is all consistent with nucleation still occurring at the twin plane even after the bottom corner of the V-groove has shifted, which in turn means that the twin plane is more favorable regarding nucleation in comparison to the step like structure of the corner geometry found at the bottom of a V-groove. This can be explained by recent work from Gamalski et al.²³ where they suggested that the nucleation barrier at a twin plane might be reduced by line energy terms. These findings show that twin planes can play an important role regarding the nucleation and growth of epitaxial layers. However, no growth is seen to initiate at the twin plane of the convex interface which would

indicate that the actual curvature of the interface plays an important role.

By comparing the relative amount of material on the {111}A- and {111}B-type facets in the profile of Figure 4B, it was possible to estimate that there is roughly 40% more material on the {111}A, suggesting a much faster growth of the {111}A-type facet. Similar conclusions have been drawn for other material systems such as InP³⁵ and GaAs²⁴ and are attributed to the polar nature of the {111}A- and {111}B-type facets and their different surface energies.^{36,37} In addition, since no incomplete overgrowth layers could be observed on the {111}A-type facets in stages I–III, the time to complete a full overgrowth layer on the {111}A-type facet is less than the time in between nucleation events whereas the opposite must apply for the {111}B-type facet.

In late stages of the overgrowth process, see Figure S1 in the Supporting Information, denoted as stage V and only found in the bottom Zb segment of the 4 Zb sample, it is no longer possible to identify the {111}-type facets. Instead, a rough disordered surface corresponding approximately to a {112}-type plane remains between adjacent {110}-type facets, with a width on the order of 5–10 nm. The roughness of the surface may very well correspond to a well ordered high index surface. We can thus conclude that, due to the noncomplete overgrowth of the TSL, the NWs will not experience a perfect hexagonal cross-section terminated by {110}-type facets; instead, small {112}-type facets remain. This is further corroborated by STM studies on Wz GaAs NWs where nanometer-sized higher index facets were observed,¹⁴ thus suggesting that this might be a general feature for NW systems of various crystal structures and material compositions.

For a better understanding of the intricate overgrowth procedure, we obtained atomically resolved images of the NW facets; see Figure 6. Figure 6E depicts a model to illustrate the relative orientation of the imaged NW facets presented in Figure 6. It should be noted that imaging of V-grooves put some challenging restrictions on the geometry and sharpness of the STM tip since it must be able to reach down to the concave interface. The {110}-type facets were found to be unreconstructed, similar to bulk {110}. A periodic change in atomic row direction occurred at each twin plane as seen in Figure 6A, but no differences in atomic appearance were observed compared to bulk samples. Imaging the {111}A-type facets in stages I–III, represented in Figure 6B, revealed rows with a separation of 0.8 nm. InAs(111)A wafers, treated in the same manner as the NWs, resulted in a (2 × 2) reconstruction as depicted in Figure 6D. The similarities between the {111}A atomic row spacing on the wafer and NW suggest that a (2 × 2) reconstruction is also present on the NW surface.

Surprisingly, high resolution images of the {111}B facet, as in Figure 6B, do not exhibit the unreconstructed (1 × 1) pattern typically found on (111)B-oriented wafers which have undergone analogous treatment, shown in Figure 6C. Instead, a quasi-periodic pattern with an approximate distance of 1–2 nm between corrugation maxima can be observed such that it is reminiscent of the ($\sqrt{19} \times \sqrt{19}$)R23.4° reconstruction commonly found on GaAs (111)B.^{38,39} Images were obtained using both positive and negative bias, and no qualitative differences were observed depending on polarity. The reconstruction has not been observed on planar InAs (111)B, and we therefore attribute it to the special confined terraces found on the NWs. Atomically resolved images were obtained on {111}B-type NW surfaces with facet widths ranging from 20

to 60 nm, all revealing a ($\sqrt{19} \times \sqrt{19}$)R23.4° like surface structure. We note that investigating NW facets outside this size regime could give insight into what degree confined terraces affect surface reconstructions, but this is not within the scope of the present study.

CONCLUSION

In conclusion, we have, using atomically resolved STM, studied homoepitaxial growth on intentionally tapered InAs NWs designed to have {111}A/B terminated twin plane superlattices. We have shown that the {111}A-type facet has a much faster growth rate in comparison to the {111}B-type facet. The overgrowth mode on the NW facets was determined to be a step flow growth. For the {111}B-type facets, the step flow growth was faster for {112}A compared to {112}B. We determine that the slower growing {111}B-type facets have a nonlinear growth rate, possibly due to a material limited growth. In addition, it was shown that overgrowth on the {111}A/B-type facets nucleates at the concave twin plane simultaneously and most probably from the same nucleus.

Thanks to the unique spatial resolution of scanning probe techniques, we were able to observe a reconstruction on InAs{111}B, not appearing on bulk samples and thus demonstrating that the atomic scale surface structure on NWs cannot always be expected to behave as on larger surfaces. The atomic surface structure is important when considering growth and modeling of core–shell NWs, since it will influence both surface energies and diffusion lengths. In addition, we have shown that epitaxial overgrowth on NW surfaces is very much affected by twin planes, and it is not unlikely that stacking faults have similar effects on the growth. Our findings allow for an increased understanding and control of radial doping profiles and material variations and self-assembly of QDs or other novel structures on NW side facets.

ASSOCIATED CONTENT

Supporting Information

STM image of Stage V, details and data related to nonlinear growth rate, details regarding growth rate vs nucleation rate calculations, and the effect of hydrogen cleaning; Figures S1–S3. This material is available free of charge via the Internet at <http://pubs.acs.org>.

AUTHOR INFORMATION

Corresponding Author

*E-mail: anders.mikkelsen@sljus.lu.se.

Notes

The authors declare no competing financial interest.

ACKNOWLEDGMENTS

This work was performed within the Nanometer Structure Consortium at Lund University (nmC@LU) and was supported by the Swedish Research Council (VR), the Swedish Foundation for Strategic Research (SSF), the Swedish energy agency, the Crafoord Foundation, the Knut and Alice Wallenberg Foundation, and the European Research Council under the European Union's Seventh Framework Programme Grant Agreement No. 259141. One of the authors (R.T.) acknowledges support from the European Commission under a Marie Curie Intra-European Fellowship. S.L. gratefully acknowledges the support by a fellowship within the Postdoc-

Programme of the German Academic Exchange Service (DAAD). We thank Daniel Jacobsson for fruitful discussions.

■ REFERENCES

- (1) Mourik, V.; Zuo, K.; Frolov, S. M.; Plissard, S. R.; Bakkers, E. P. A. M.; Kouwenhoven, L. P. Signatures of Majorana Fermions in Hybrid Superconductor-Semiconductor Nanowire Devices. *Science* **2012**, *336*, 1003–1007.
- (2) Das, A.; Ronen, Y.; Most, Y.; Oreg, Y.; Heiblum, M.; Shtrikman, H. Zero-Bias Peaks and Splitting in an Al-InAs Nanowire Topological Superconductor as a Signature of Majorana Fermions. *Nat. Phys.* **2012**, *8*, 887–895.
- (3) Hochbaum, A. I.; Yang, P. Semiconductor Nanowires for Energy Conversion. *Chem. Rev.* **2009**, *110*, 527–546.
- (4) Egard, M.; Johansson, S.; Johansson, A. C.; Persson, K. M.; Dey, A. W.; Borg, B. M.; Thelander, C.; Wernersson, L. E.; Lind, E. Vertical InAs Nanowire Wrap Gate Transistors with $F_t > 7$ Ghz and $F_{max} > 20$ Ghz. *Nano Lett.* **2010**, *10*, 809–812.
- (5) Saxena, D.; Mokkapati, S.; Parkinson, P.; Jiang, N.; Gao, Q.; Tan, H. H.; Jagadish, C. Optically Pumped Room-Temperature GaAs Nanowire Lasers. *Nat. Photonics* **2013**, *7*, 963–968.
- (6) Yan, R.; Gargas, D.; Yang, P. Nanowire Photonics. *Nat. Photonics* **2009**, *3*, 569–576.
- (7) Wallentin, J.; Anttu, N.; Asoli, D.; Huffman, M.; Åberg, I.; Magnusson, M. H.; Siefer, G.; Fuss-Kaiulweit, P.; Dimroth, F.; Witzigmann, B.; Xu, H. Q.; Samuelson, L.; Deppert, K.; Borgström, M. T. InP Nanowire Array Solar Cells Achieving 13.8% Efficiency by Exceeding the Ray Optics Limit. *Science* **2013**, *339*, 1057–1060.
- (8) Jiang, N.; Gao, Q.; Parkinson, P.; Wong-Leung, J.; Mokkapati, S.; Breuer, S.; Tan, H. H.; Zheng, C. L.; Etheridge, J.; Jagadish, C. Enhanced Minority Carrier Lifetimes in GaAs/AlGaAs Core–Shell Nanowires through Shell Growth Optimization. *Nano Lett.* **2013**, *13*, 5135–5140.
- (9) Heiss, M.; Fontana, Y.; Gustafsson, A.; Wüst, G.; Magen, C.; O'Regan, D. D.; Luo, J. W.; Ketterer, B.; Conesa-Boj, S.; Kuhlmann, A. V.; Houel, J.; Russo-Averchi, E.; Morante, J. R.; Cantoni, M.; Marzari, N.; Arbiol, J.; Zunger, A.; Warburton, R. J.; Fontcuberta i Morral, A. Self-Assembled Quantum Dots in a Nanowire System for Quantum Photonics. *Nat. Mater.* **2013**, *12*, 439–444.
- (10) Vu, T. T. T.; Zehender, T.; Verheijen, A. M.; Plissard, R. S.; Immink, W. G. G.; Haverkort, E. M. J.; Bakkers, P. A. M. E. High Optical Quality Single Crystal Phase Wurtzite and Zincblende InP Nanowires. *Nanotechnology* **2013**, *24*, 115705.
- (11) Guo, Y.-N.; Burgess, T.; Gao, Q.; Tan, H. H.; Jagadish, C.; Zou, J. Polarity-Driven Nonuniform Composition in InGaAs Nanowires. *Nano Lett.* **2013**, *13*, 5085–5089.
- (12) Zheng, C.; Wong-Leung, J.; Gao, Q.; Tan, H. H.; Jagadish, C.; Etheridge, J. Polarity-Driven 3-Fold Symmetry of GaAs/AlGaAs Core Multishell Nanowires. *Nano Lett.* **2013**, *13*, 3742–3748.
- (13) Hilner, E.; Hakanson, U.; Froberg, L. E.; Karlsson, M.; Kratzer, P.; Lundgren, E.; Samuelson, L.; Mikkelsen, A. Direct Atomic Scale Imaging of III-V Nanowire Surfaces. *Nano Lett.* **2008**, *8*, 3978–3982.
- (14) Hjort, M.; Lehmann, S.; Knutsson, J.; Timm, R.; Jacobsson, D.; Lundgren, E.; Dick, K. A.; Mikkelsen, A. Direct Imaging of Atomic Scale Structure and Electronic Properties of GaAs Wurtzite and Zinc Blende Nanowire Surfaces. *Nano Lett.* **2013**, *13*, 4492–4498.
- (15) Xu, T.; Dick, K. A.; Plissard, S.; Nguyen, T. H.; Makoudi, Y.; Berthe, M.; Nys, J. P.; Wallart, X.; Grandidier, B.; Caroff, P. Faceting, Composition and Crystal Phase Evolution in III-V Antimonide Nanowire Heterostructures Revealed by Combining Microscopy Techniques. *Nanotechnology* **2012**, *23*, 095702.
- (16) Hjort, M.; Wallentin, J.; Timm, R.; Zakharov, A. A.; Håkanson, U.; Andersen, J. N.; Lundgren, E.; Samuelson, L.; Borgström, M. T.; Mikkelsen, A. Surface Chemistry, Structure, and Electronic Properties from Microns to the Atomic Scale of Axially Doped Semiconductor Nanowires. *ACS Nano* **2012**, *6*, 9679–9689.
- (17) Timm, R.; Persson, O.; Engberg, D. L. J.; Fian, A.; Webb, J. L.; Wallentin, J.; Jönsson, A.; Borgström, M. T.; Samuelson, L.; Mikkelsen, A. Current–Voltage Characterization of Individual as-grown Nanowires Using a Scanning Tunneling Microscope. *Nano Lett.* **2013**, *13*, 5182–5189.
- (18) Cui, Y.; Wang, J.; Plissard, S. R.; Cavalli, A.; Vu, T. T. T.; van Veldhoven, R. P. J.; Gao, L.; Trainor, M.; Verheijen, M. A.; Haverkort, J. E. M.; Bakkers, E. P. A. M. Efficiency Enhancement of InP Nanowire Solar Cells by Surface Cleaning. *Nano Lett.* **2013**, *13*, 4113–4117.
- (19) Fengyun, W.; SenPo, Y.; Ning, H.; KitWa, F.; Hao, L.; Jared, J. H.; Guofa, D.; TakFu, H.; Chan, K. S.; Johnny, C. H. Surface Roughness Induced Electron Mobility Degradation in InAs Nanowires. *Nanotechnology* **2013**, *24*, 375202.
- (20) Hjort, M.; Lehmann, S.; Knutsson, J.; Zakharov, A. A.; Du, Y. A.; Sakong, S.; Timm, R.; Nylund, G.; Lundgren, E.; Kratzer, P.; Dick, K. A.; Mikkelsen, A. Electronic and Structural Differences between Wurtzite and Zinc Blende InAs Nanowire Surfaces: Experiment and Theory. *ACS Nano* **2014**, *8*, 12346–12355.
- (21) Caroff, P.; Dick, K. A.; Johansson, J.; Messing, M. E.; Deppert, K.; Samuelson, L. Controlled Polytypic and Twin-Plane Superlattices in III-V Nanowires. *Nat. Nanotechnol.* **2009**, *4*, 50–55.
- (22) Algra, R. E.; Verheijen, M. A.; Borgstrom, M. T.; Feiner, L.-F.; Immink, G.; van Enckevort, W. J. P.; Vlieg, E.; Bakkers, E. P. A. M. Twinning Superlattices in Indium Phosphide Nanowires. *Nature* **2008**, *456*, 369–372.
- (23) Gamalski, A. D.; Voorhees, P. W.; Ducati, C.; Sharma, R.; Hofmann, S. Twin Plane Re-Entrant Mechanism for Catalytic Nanowire Growth. *Nano Lett.* **2014**, *14*, 1288–1292.
- (24) Burgess, T.; Breuer, S.; Caroff, P.; Wong-Leung, J.; Gao, Q.; Hoe Tan, H.; Jagadish, C. Twinning Superlattice Formation in GaAs Nanowires. *ACS Nano* **2013**, *7*, 8105–8114.
- (25) Hamilton, D. R.; Seidensticker, R. G. Propagation Mechanism of Germanium Dendrites. *J. Appl. Phys.* **1960**, *31*, 1165–1168.
- (26) van de Waal, B. W. Cross-Twinning Model of fcc Crystal Growth. *J. Cryst. Growth* **1996**, *158*, 153–165.
- (27) Biasiol, G.; Gustafsson, A.; Leifer, K.; Kapon, E. Mechanisms of Self-Ordering in Nonplanar Epitaxy of Semiconductor Nanostructures. *Phys. Rev. B* **2002**, *65*, 205306.
- (28) Gustafsson, A.; Reinhardt, F.; Biasiol, G.; Kapon, E. Low-Pressure Organometallic Chemical Vapor Deposition of Quantum Wires on V-Grooved Substrates. *Appl. Phys. Lett.* **1995**, *67*, 3673–3675.
- (29) Ishida, S.; Arakawa, Y.; Wada, K. Seeded Self-Assembled GaAs Quantum Dots Grown in Two-Dimensional V Grooves by Selective Metal–Organic Chemical-Vapor Deposition. *Appl. Phys. Lett.* **1998**, *72*, 800–802.
- (30) Magnusson, M. H.; Deppert, K.; Malm, J.-O.; Bovin, J.-O.; Samuelson, L. Size-Selected Gold Nanoparticles by Aerosol Technology. *Nanostruct. Mater.* **1999**, *12*, 45–48.
- (31) Lehmann, S.; Jacobsson, D.; Deppert, K.; Dick, K. A. High Crystal Quality Wurtzite-Zinc Blende Heterostructures in Metal-Organic Vapor Phase Epitaxy-Grown GaAs Nanowires. *Nano Res.* **2012**, *5*, 470–476.
- (32) Lehmann, S.; Wallentin, J.; Jacobsson, D.; Deppert, K.; Dick, K. A. A General Approach for Sharp Crystal Phase Switching in InAs, GaAs, InP, and GaP Nanowires Using Only Group V Flow. *Nano Lett.* **2013**, *13*, 4099–4105.
- (33) Michely, T.; Hohage, M.; Bott, M.; Comsa, G. Inversion of Growth Speed Anisotropy in Two Dimensions. *Phys. Rev. Lett.* **1993**, *70*, 3943–3946.
- (34) Hilner, E.; Lundgren, E.; Mikkelsen, A. Surface Structure and Morphology of InAs(111)B with/without Gold Nanoparticles Annealed under Arsenic or Atomic Hydrogen Flux. *Surf. Sci.* **2010**, *604*, 354–360.
- (35) Ghalamestani, S. G.; Heurlin, M.; Wernersson, L. E.; Lehmann, S.; Dick, K. A. Growth of InAs/InP Core–Shell Nanowires with Various Pure Crystal Structures. *Nanotechnology* **2012**, *23*, 285601.
- (36) Moll, N.; Kley, A.; Pehlke, E.; Scheffler, M. GaAs Equilibrium Crystal Shape from First Principles. *Phys. Rev. B* **1996**, *54*, 8844–8855.
- (37) Zou, J.; Paladugu, M.; Wang, H.; Auchterlonie, G. J.; Guo, Y.-N.; Kim, Y.; Gao, Q.; Joyce, H. J.; Tan, H. H.; Jagadish, C. Growth

Mechanism of Truncated Triangular III–V Nanowires. *Small* **2007**, *3*, 389–393.

(38) Thornton, J. M. C.; Woolf, D. A.; Weightman, P. Reconstructions of the GaAs(111)B Surface. *Appl. Surf. Sci.* **1998**, *123*, 115–119.

(39) Farrell, H. H.; Lu, J.; Schultz, B. D.; Denison, A. B.; Palmstrøm, C. J. GaAs(111)B($\sqrt{19} \times \sqrt{19}$)R23.4° Surface Reconstruction. *J. Vac. Sci. Technol., B* **2001**, *19*, 1597–1605.